Journal of
Materials Chemistry A

ROYAL SOCIETY
OF CHEMISTRY

PAPER

View Article Online
View Journal

Check for updates

Cite this: DOI: 10.1039/d6ta01590e

Open Access Article. Published on 13 May 2026. Downloaded on 6/3/2026 11:05:26 AM.
This article is licensed under a Creative Commons Attribution 3.0 Unported Licence.

Spacer cation electronic structure controls excited-state pathways in two-dimensional hybrid perovskites

Camryn J. Gloor, Zijian Gan, Jordan Shanahan, William A. Hearne, Chun-Hsing Chen, Sampreeti Bhattacharya, Jun Hu, Liang Yan, Yosuke Kanai, Andrew M. Moran * and Wei You *

Received 22nd February 2026
Accepted 13th May 2026

DOI: 10.1039/d6ta01590e

rsc.li/materials-a

Conjugated organic cations have been explored in two-dimensional (2D) organic–inorganic hybrid perovskites (OIHPs) due to tunable optoelectronic functionality of such hybrid materials. However, relatively few conjugated organic cations have been successfully incorporated into 2D OIHPs, and many exhibit relatively large optical band gaps (2.5 eV or larger), largely due to constraints associated with cation size and solubility. Here, we investigate how the spacer-cation electronic structure biases excited-state pathways in 2D OIHPs using a series of compact, tetrazine-based organic cations with narrow optical gaps (~2.1 eV) that are successfully incorporated into lead-based 2D perovskites *via* solution processing. Mixed-anion thin films (50% Br and 50% Cl) are used to shift the inorganic exciton into the visible spectral range, enabling spectroscopic investigation of excited-state processes. Steady-state photoluminescence reveals strong quenching of the inorganic emission, consistent with charge- and/or energy-transfer processes. Spacer-cation-dependent behavior is further examined using photoluminescence excitation (PLE) and transient grating (TG) spectroscopy, which indicate that $[\mathrm{MeTzPMA}]_2\mathrm{PbBr}_2\mathrm{Cl}_2$ and $[\mathrm{MeTzEA}]_2\mathrm{PbBr}_2\mathrm{Cl}_2$ favor short-range, Dexter-type energy transfer in competition with charge separation, while $[\mathrm{MePTzEA}]_2\mathrm{PbBr}_2\mathrm{Cl}_2$ exhibits quenching dominated by charge transfer. Overall, these results reveal spacer-cation electronic structure as a key design parameter for regulating short-range interfacial coupling and excited-state pathways in 2D hybrid perovskites, providing useful principles for tailoring optoelectronic functionality.

Introduction

Two-dimensional (2D) organic–inorganic hybrid perovskites (OIHPs) have attracted significant attention because of their tunable optoelectronic properties and diverse physical properties.[1–8] A defining feature of 2D OIHPs is the incorporation of organic spacer-cations between the inorganic slabs, which enables systematic control of their optoelectronic properties through chemical design.[5–14] Recent studies have shown that the coupling between the organic spacer-cation and inorganic sublattice can strongly influence carrier dynamics and electron–phonon interactions.[15] In addition, mismatches in the dielectric constants and electronic structures at the inorganic/organic interfaces lead to electron and hole confinement within 2D quantum wells, resulting in low out-of-plane conductivity.[16–18] Importantly, careful selection of the organic component can alter the band alignment between quantum wells and organic layers (Fig. S1) through adjustment of the spacer-cation's energy levels (*i.e.*, the highest occupied molecular orbital (HOMO) and lowest unoccupied molecular orbital (LUMO)), thereby enabling control over exciton localization and charge separation.[8,10,11,17,19]

Depending on the relative alignment of organic and inorganic energy levels, distinct interfacial alignment configurations can be accessed in 2D OIHPs. In type-I alignments, one band straddles the other with excitons remaining localized within either the organic (type-Ia) or inorganic (type-Ib) component, whereas type-II alignments feature staggered energy levels that facilitate carrier separation. Achieving control over these alignments requires careful design of the organic spacer-cation. To date, oligo(thiophene)s and acenes have been successfully incorporated into 2D OIHPs, most commonly adopting type-Ib alignment due to the rather large band gap of these organics.[8,17,20–22] In contrast, examples of type-Ia and type-II alignments remain comparatively rare, largely owing to the scarcity of suitably small, narrow-band-gap organic cations compatible with the structural requirements of 2D perovskites.[2,8,10,11,20,21,23–30]

Although the design and synthesis of small band gap conjugated organic molecules have been widely explored in other contexts,[31–34] translating these strategies to 2D OIHPs

---

Department of Chemistry, University of North Carolina at Chapel Hill, Chapel Hill, NC 27599-3290, USA. E-mail: wyou@unc.edu

Open Access Article. Published on 13 May 2026. Downloaded on 6/3/2026 11:05:26 AM.
This article is licensed under a Creative Commons Attribution 3.0 Unported Licence.

presents unique challenges. The inorganic lattice sets a strict width constraint for the organic component (*i.e.*, 8.4 Å for lead iodide-based OIHPs), while longer organic molecules suffer from limited solubility in common OIHP processing solvents such as DMSO. For instance, extending the conjugation of oligo(thiophene)s by adding more thiophene repeat units can reduce the optical band gap, but typically requires long and/or bulky side chains to maintain solubility, which in turn increases molecular dimensions beyond the lattice compatibility.[35–37] Another common strategy is to apply the 'donor–acceptor' concept to achieve conjugated organics of shorter length yet having smaller band gaps. While this strategy has been widely used in conjugated polymers,[38] identifying donor–acceptor motifs that simultaneously satisfy electronic, structural, and processing constraints for 2D OIHPs remains nontrivial. In particular, short-range type-II energy transfer, which requires direct orbital overlap, is expected to be highly sensitive to spacer-cation proximity and electronic structure, in contrast to longer-range Förster-type energy transfer governed by dipole–dipole coupling.

Tetrazine-based conjugated molecules are attractive in this context, as they can achieve narrow optical band gaps with just 1–3 aromatic units,[39–41] and exhibit optical and electronic features distinct from many spacer-cations previously explored in 2D OIHPs. Specifically, tetrazine derivatives exhibit a low-energy optical transition in the yellow-orange spectral region,[39–41] whereas acene- and thiophene-derivatives typically require 3–5 rings to achieve comparable low-energy transitions.[42,43] With the incorporation of nitrogen atoms in the structure of tetrazine, the frontier orbitals are shifted from π–π^*—common to benzene-derivatives—to n–π^*, resulting in a narrowing of the HOMO–LUMO band gap. Notably, a higher energy π–π^* transition in the near-UV range is also present for these tetrazine-based molecules. Collectively, these features position tetrazine derivatives as promising spacer-cations for probing excited-state pathways in 2D OIHPs, although such systems remain relatively unexplored.[44]

Herein, we investigate how the electronic structure of the spacer-cation influences excited-state pathways in 2D hybrid perovskites using a series of compact, tetrazine-based organic cations as a model system. These cations are incorporated into lead-chloride and mixed-anion (50% Br and 50% Cl) 2D OIHP thin films and single crystals, enabling systematic variation of conjugation length and connectivity, while maintaining narrow HOMO–LUMO gaps of the cations. Mixed-anion compositions are employed to tune interfacial energetics and assess their impact on competing excited-state pathways. Ultraviolet photoelectron spectroscopy (UPS) measurements indicate a type-II band alignment between organic and inorganic components in these systems. Through steady-state photoluminescence studies, we observe a quenching of emission, indicative of excited-state relaxation pathways involving charge and/or energy transfer. Complementary photoluminescence excitation (PLE) and transient grating (TG) spectroscopy are then used to resolve cation-dependent excited-state behavior.

Experimental methods

The tetrazine-based organic cations 2-(6-methyl-1,2,4,5-tetrazin-3-yl)ethan-1-aminium (MeTzEA), 2-(6-(*p*-tolyl)-1,2,4,5-tetrazin-3-yl)ethan-1-aminium (MePTzEA), and (4-(6-methyl-1,2,4,5-tetrazin-3-yl)phenyl)methanaminium (MeTzPMA) were synthesized following modified literature procedures.[45] The corresponding chloride salts were obtained by treatment of the amine precursors with 2 M HCl in dry diethyl ether. Thin films of tetrazine-based 2D organic–inorganic hybrid perovskites were prepared by spin coating precursor solutions containing the appropriate organic ammonium chloride salt and $PbCl_2$ (or $PbBr_2$ for mixed-anion films) in DMSO at a 2 : 1 molar ratio onto precleaned glass substrates. Thin-film deposition conditions (spin-coating speed and annealing conditions) were adjusted to optimize film formation due to differences in solubility and crystallization behavior. Powder X-ray diffraction (pXRD) measurements were collected to confirm the layered 2D perovskite structure and interlayer spacing of all thin films. The resulting films have typical thicknesses of 50–60 nm for MeTzEA based films, 90–120 nm for MePTzEA based films, and 90–110 nm for MeTzPMA based films as measured by profilometry.

Single crystals of $[MeTzEA]_2PbCl_4$, $[MeTzPMA]_2PbCl_4\cdot CH_2Cl_2$, and $[MePTzEA]_2PbCl_4$ were grown using an antisolvent vapor-assisted crystallization (AVC) method. Mixed-anion single crystals of $[BA]_2PbBr_2Cl_2$ and $[MeTzEA]_2PbBr_2Cl_2$ were grown using analogous procedures. Single-crystal X-ray diffraction data were collected on a Bruker diffractometer, and structures were solved using standard refinement protocols. Crystallographic parameters and additional structural details are provided in the SI.

Density functional theory (DFT) calculations were performed using the all-electron FHI-aims code, following previously reported protocols.[17,46,47] Structural models were based on experimentally determined crystal structures. Further computational details, including basis sets and exchange–correlation functionals, are provided in the SI (Section S6).

Ultraviolet photoelectron spectroscopy (UPS) measurements were performed to determine valence band positions of both organic and inorganic components. Thin films of BA-based perovskites deposited on silicon wafers were used to determine inorganic bands, while thin films of organic ammonium salts deposited on silicon wafers were prepared to determine organic HOMO levels. The secondary electron cutoff and valence band onset were used to determine HOMO and valence band energies. Optical gaps obtained from UV-visible spectroscopy were used to estimate conduction band and LUMO positions.

UV-visible absorption spectra of thin films were collected using a Shimadzu UV-2600 spectrometer. All UV-Vis absorption measurements were performed under identical experimental conditions, including substrate type and ambient temperature. Spectra were normalized to facilitate comparison across the series. Scanning electron microscopy (SEM) images were collected using a Zeiss SUPRA 25 field-emission scanning electron microscope at an accelerating voltage of 2.0 kV. Films were

Open Access Article. Published on 13 May 2026. Downloaded on 6/3/2026 11:05:26 AM.
This article is licensed under a Creative Commons Attribution 3.0 Unported Licence.

imaged as prepared on glass substrates without additional coating. X-ray photoelectron spectroscopy (XPS) data were collected on a Kratos Supra+ system with a monochromatic Kα X-ray source operated at 150 W. Films were measured as prepared on glass substrates without additional coating. Additional information pertaining to SEM and XPS experiments can be found in the SI.

Steady-state photoluminescence (PL) measurements were performed using excitation wavelengths selected to preferentially excite the inorganic or organic component. Photoluminescence excitation (PLE) spectra were recorded by monitoring emission at a wavelength corresponding to tetrazine n–π* emission (600 nm) while scanning the excitation wavelength across 330 nm to 550 nm. Femtosecond transient grating (TG) experiments were conducted using 375 nm pump and probe pulses to selectively excite the inorganic exciton of the 2D perovskites. Signal fields were detected using spectral interferometry to enhance sensitivity to excited-state population dynamics. Data were analyzed by fitting the signal amplitude to multi-exponential decay functions to extract characteristic relaxation time constants. Full experimental details and fitting procedures are provided in the SI (Sections S8 and S9).

Results and discussion

Design and optical properties of tetrazine-based organic cations

We synthesized three tetrazine-based organic ammoniums, 2-(6-methyl-1,2,4,5-tetrazin-3-yl)ethan-1-aminium (MeTzEA), 2-(6-(*p*-tolyl)-1,2,4,5-tetrazin-3-yl)ethan-1-aminium (MePTzEA), and (4-(6-methyl-1,2,4,5-tetrazin-3-yl)phenyl)methanaminium (MeTzPMA) (Fig. 1A, S2–S7 and Scheme S1). The MeTzEA and MePTzEA (with one more benzene unit than MeTzEA) cations differ in their overall length, with a length of 7.1 Å for MeTzEA and 11.8 Å for MePTzEA. Correspondingly, the interlayer spacing in the resulting 2D OIHPs increases from 15.8 Å for MeTzEA to 23.6 Å for MePTzEA, as determined from powder X-ray diffraction of thin films. In contrast, MeTzPMA and MePTzEA are similar in length (10.2 Å for MeTzPMA and 11.8 Å for MePTzEA), leading to comparable quantum-well spacings of 19.3 Å and 22.9 Å, respectively. However, these two cations differ in their connectivity, altering the position of the electron-withdrawing tetrazine ring relative to the inorganic layer. In MePTzEA, the tetrazine moiety is closer to the inorganic layer in the putative 2D structure, a geometric difference that is expected to influence charge distribution and interfacial coupling between the organic and inorganic components. Overall, variations in spacer-cation length and connectivity provide a means to tune interlayer coupling and interfacial interactions in these systems.

This series enables evaluation of how the tetrazine moiety, conjugation length, and connectivity influence band alignment and optoelectronic properties in 2D OIHPs. For all three systems, chloride salts were synthesized *via* reaction with dry hydrogen chloride, and the resulting precursors were used to fabricate the corresponding 2D OIHP thin films as detailed in the SI (Section 3.2 and Fig. S8).

The synthesized organic ammonium salts exhibit sufficient solubility in DMSO, a common processing solvent for 2D OIHPs. In solution, the tetrazine salts exhibit two distinct absorption bands (Fig. 1B). The low-energy transition corresponds to the tetrazine n–π* transition from 450 nm to 600 nm, resulting in a band gap of 2.1 eV. Notably, because the tetrazine moiety is responsible for this low-energy transition, the length of conjugation does not affect the optical gap, making the tetrazine group an unusual case. In contrast, the high-energy absorption region, which includes contributions from the tetrazine π–π* transition and the aromatic substituents, varies across the series. MeTzEACl shows an absorption onset near 325 nm, whereas MeTzPMACl and MePTzEACl exhibit broader bands extending to 375 and 385 nm, respectively. The differences can be attributed to the addition of the benzene group, which also absorbs in this region, resulting in a shoulder around 350 nm and an increase of absorbance below 300 nm for MeTzPMACl and MePTzEACl.

The photoluminescence (PL) spectra of the three salts are also similar and extend from 550 to 700 nm when excited at both 320 nm and 510 nm (Fig. 1C). Notably, MeTzEACl exhibits

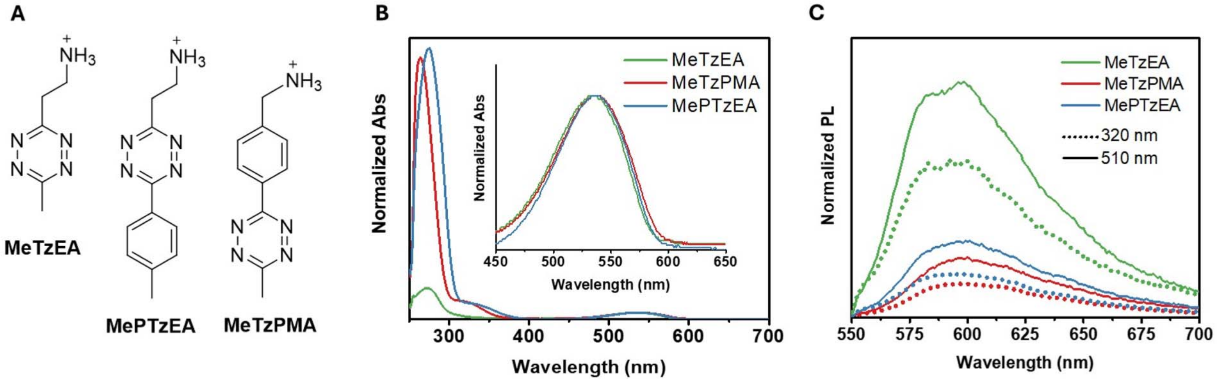

Fig. 1 Tetrazine-based salts and their optical properties in solution. (A) Chemical structures of the tetrazine-based ammonium cations synthesized in this work. (B) Absorbance of tetrazine salts in DMSO normalized to the low-energy n–π* transition. Inset shows the low-energy n–π* transition from 450 nm to 650 nm. (C) Photoluminescence (PL) of the tetrazine salts in DMSO, normalized for the number of photons absorbed, with an excitation wavelength of 320 nm (dotted line) and 510 nm (solid line).

Open Access Article. Published on 13 May 2026. Downloaded on 6/3/2026 11:05:26 AM.
This article is licensed under a Creative Commons Attribution 3.0 Unported Licence.

higher emission intensity than MeTzPMA and MePTzEA, both of which have a benzene unit as part of the organic cation. Phenyl substitution on tetrazine likely reduces the spatial overlap between the localized nonbonding orbital and the delocalized π* orbital, thereby diminishing the transition dipole moment for the n–π* transition and reducing its intensity in emission. Nevertheless, as revealed below, having the benzene unit in the organic cations does not appear to affect the observed PL in all three organic cation-based 2D OIHPs.

Crystal structures and packing motifs in tetrazine-based 2D OIHPs

Through the antisolvent vapor-assisted crystallization (AVC) method (Fig. S9),[48] we obtained tetrazine-based perovskite crystals of the three hybrid materials, namely $[MeTzEA]_2PbCl_4$, $[MeTzPMA]_2PbCl_4\cdot CH_2Cl_2$, and $[MePTzEA]_2PbCl_4$. Single-crystal X-ray diffraction was used to confirm their two-dimensional perovskite structures and to examine how spacer-cation length and connectivity influence packing within the organic layers. Representative crystal images are shown in Fig. S10, and key crystallographic parameters are summarized in Tables S2–S4, with full details provided in the SI. Side views of the structures are displayed in Fig. 2. All three compounds crystallize as layered perovskites consisting of corner-sharing octahedra ($[PbCl_6]^{4-}$) separated by organic bilayers. Specifically, $[MeTzEA]_2PbCl_4$ crystals adopt a monoclinic, *C*2/*m* space group (Fig. 2A and B), $[MeTzPMA]_2PbCl_4\cdot CH_2Cl_2$ crystals adopt an orthorhombic, $Pca2_1$ space group (Fig. 2C and D), and the $[MePTzEA]_2PbCl_4$ crystals adopt a monoclinic, *Cc* space group (Fig. 2E and F). Despite these differences in symmetry, all three structures share similar inorganic frameworks, while variations in cation length and connectivity lead to distinct packing motifs within the organic layers.

The arrangements of the tetrazine cations differ among the three crystal structures, reflecting differences in cation length and connectivity. In $[MeTzEA]_2PbCl_4$, the tetrazine unit exhibits positional disorder about a twofold rotation axis, with one representative configuration shown in Fig. 2A and B. When viewed along the *a*-axis, the organic cations form an ordered vertical stack (Fig. 2A). Viewing along the *c*-axis reveals that the cations are rotated in the same direction, resulting in terminal methyl groups oriented toward neighboring tetrazine rings (Fig. 2B), consistent with a T-shaped π–π stacking motif. Owing to its shorter molecular length, MeTzEA yields the smallest interlayer spacing in the series, with a quantum-well distance of 15.8 Å, compared to 23.6 Å and 22.9 Å for the MePTzEA and MeTzPMA based structures, respectively.

Incorporation of a phenyl ring significantly alters the packing arrangement within the organic layers. Specifically, in $[MeTzPMA]_2PbCl_4\cdot CH_2Cl_2$, tetrazine cations stack in groups of four, separated by two dichloromethane molecules located near the tetrazine rings (Fig. 2C and D). By contrast, in $[MePTzEA]_2PbCl_4$, the cations again align vertically (Fig. 2E) but are rotated in alternating directions within the organic layer, leading to a staggered formation. In addition, adjacent tetrazine moieties are tilted, giving rise to a herringbone configuration within the organic layer (Fig. 2F). Additional structural orientations are provided in Fig. S11–S13.

It is worth noting that in $[MeTzPMA]_2PbCl_4\cdot CH_2Cl_2$, the presence of dichloromethane results in a clustered arrangement of tetrazine cations, in contrast to the more uniform alignment observed in the non-solvated structures. Attempts to grow MeTzPMA-based crystals without incorporating dichloromethane were unsuccessful despite varying crystallization conditions. Accordingly, comparisons of packing trends across the series must be considered in the context of solvent inclusion in this structure.

Thin-film structure and optical absorption

While single crystal analysis provides detailed insight into structural features such as packing and intermolecular interactions, thin films are more directly relevant for probing

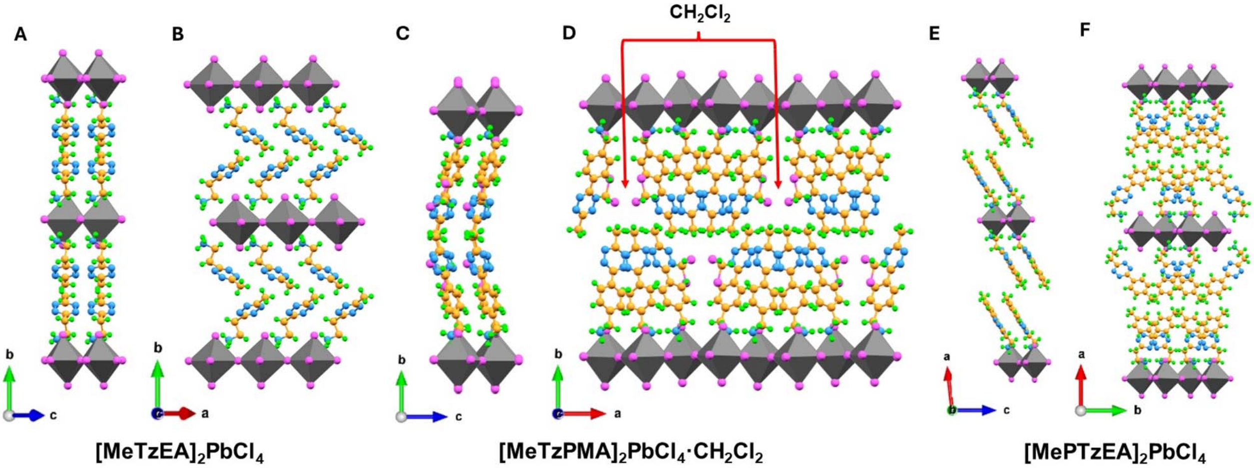

Fig. 2 Side views of the crystal structures. $[MeTzEA]_2PbCl_4$ viewed down (A) *a*-axis and (B) *c*-axis. $[MeTzPMA]_2PbCl_4\cdot CH_2Cl_2$ viewed down (C) *a*-axis and (D) *c*-axis; dichloromethane molecules present in the lattice are indicated by red arrows. $[MePTzEA]_2PbCl_4$ viewed down (E) *b*-axis and (F) *c*-axis. Cl, magenta; C, orange; N, blue; H, green; gray diamonds within inorganic layers represent octahedral $[PbCl_6]^{4-}$.

Open Access Article. Published on 13 May 2026. Downloaded on 6/3/2026 11:05:26 AM.
This article is licensed under a Creative Commons Attribution 3.0 Unported Licence.

optoelectronic properties. Thin films of the three tetrazine-based perovskites were prepared from precursor solutions of the corresponding ammonium salts and $PbCl_2$ in DMSO. The resulting films exhibit strong layered type diffraction, consistent with the formation of a 2D structure (Fig. 3A). The UV-Vis spectra of such films demonstrate absorption features from both the organic and inorganic components (Fig. 3B). The raw absorbance spectra for these films are shown in Fig. S16. Specifically, MeTzEACl-based film has a sharp exciton absorption peak at 344 nm, whereas the films incorporating MeTzPMACl and MePTzEACl display excitonic absorption peaks at 337 nm and 334 nm, respectively. The slight blue shift in the absorption peak is consistent with an increased distortion of the inorganic framework because of the larger cation size in the latter two cases. Importantly, all three films exhibit additional absorption in the 500–600 nm region, corresponding to the n–π* transition of the tetrazine moiety, confirming the successful incorporation of the conjugated cations into the perovskite lattice. Together, these observations establish that the tetrazine-based cations are retained within the 2D perovskite thin films, providing a platform to examine their influence on excited-state behavior.

Mixed-anion compositions for spectroscopic access

Experimentally, the different band alignments between the organic and inorganic components are generally evaluated using a combination of electronic structure calculations and spectroscopy.[10,11,17,19,49] While the chloride-based tetrazine perovskites establish key structural and electronic trends, mixed-anion compositions provide improved spectroscopic access to the inorganic exciton by shifting its absorption into the visible region. Accordingly, mixed-anion (50% Br and 50% Cl) 2D OIHP thin films were employed to enable systematic optical and electronic interrogation of excited-state processes. X-ray photoelectron spectroscopy (XPS) analysis confirms incorporation of both Cl and Br in all samples, with compositions close to the intended 1 : 1 ratio (Fig. S17 and Table S1). The measured Br : Cl ratios are consistent across independently prepared films and show minimal variation with shallow sputtering, indicating uniform halide distribution.

The UV-Vis spectra of the 50% Br/50% Cl 2D OIHP films retain contributions from both the inorganic framework and the organic spacer-cations (Fig. 4A). Incorporation of bromide results in a clear red shift of the inorganic exciton absorption relative to the fully chloride analogues. For example, $[MeTzEA]_2PbBr_2Cl_2$ exhibits a sharp excitonic absorption peak at 378 nm, compared to 344 nm for the fully chloride analogue, $[MeTzEA]_2PbCl_4$. Similar shifts are observed for the other mixed-anion films, with excitonic peaks shifting from 337 to 370 nm for MeTzPMA and from 334 to 365 nm for MePTzEA. Importantly, all three mixed-anion perovskites also retain the characteristic tetrazine n–π* absorption between 500 and 600 nm. Powder X-ray diffraction patterns (Fig. 4B) confirm that the mixed-anion films preserve pronounced layered ordering. Comparison with the chloride-only films reveals negligible changes in interlayer spacing (Fig. S18C), indicating that partial halide substitution does not substantially alter the periodicity of the inorganic framework.

SEM images of the films (Fig. S19), collected over multiple length scales, show largely continuous and uniform morphologies across all three compositions, with no well-defined grain structures observed even at higher magnification. While minor variations in surface texture are present, the overall similarity in film morphology suggests that the observed differences in excited-state dynamics are not primarily driven by morphological effects. Additionally, while halide phase segregation is a known concern in mixed-halide perovskites, no evidence of phase separation is observed in the present system. The absorption spectra exhibit a single excitonic feature for each composition, and the pXRD patterns show a single set of reflections without peak splitting. These observations indicate that any compositional heterogeneity, if present, does not lead to distinct optoelectronic domains.

Because changes in anion composition can influence crystal packing and local structure, mixed-anion single crystals of

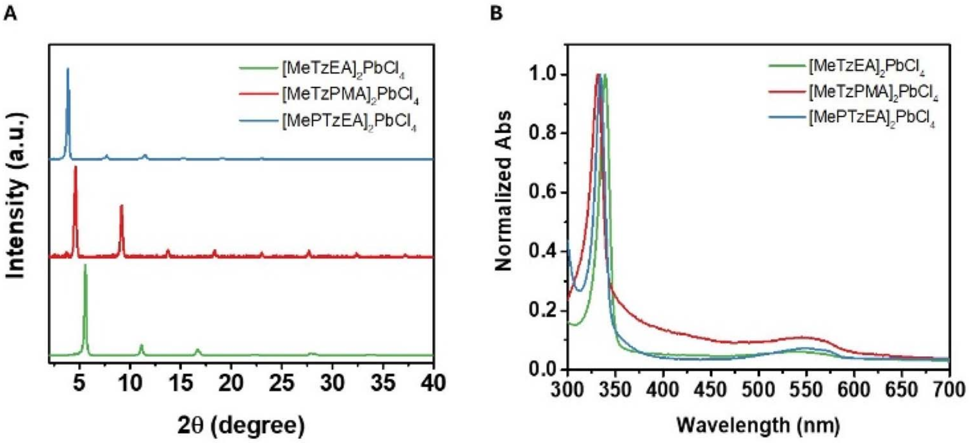

Fig. 3 Characterization of tetrazine-based lead chloride 2D OIHP thin films. (A) Measured powder X-ray diffraction pattern (pXRD) of perovskite thin films for $[MeTzEA]_2PbCl_4$ (green), $[MeTzPMA]_2PbCl_4$ (red), and $[MePTzEA]_2PbCl_4$ (blue). (B) Normalized UV-Vis absorbance of $[MeTzEA]_2PbCl_4$ (green), $[MeTzPMA]_2PbCl_4$ (red), and $[MePTzEA]_2PbCl_4$ (blue) thin films.

Open Access Article. Published on 13 May 2026. Downloaded on 6/3/2026 11:05:26 AM.
This article is licensed under a Creative Commons Attribution 3.0 Unported Licence.

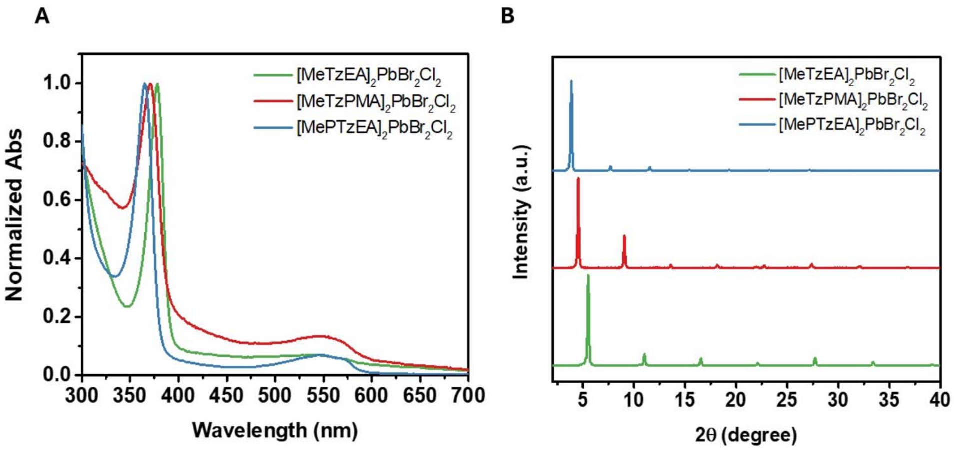

Fig. 4 Characterization of tetrazine-based mixed-anion 2D OIHP thin films. (A) Normalized UV-Vis absorbance of $[MeTzEA]_2PbBr_2Cl_2$ (green), $[MeTzPMA]_2PbBr_2Cl_2$ (red), and $[MePTzEA]_2PbBr_2Cl_2$ (blue) thin films. (B) Measured powder X-ray diffraction pattern (pXRD) of the mixed-anion perovskite thin films.

$[BA]_2PbBr_2Cl_2$ and $[MeTzEA]_2PbBr_2Cl_2$ were selectively grown to enable comparison with the fully chloride systems. Single-crystal X-ray diffraction confirms that both mixed-anion structures retain the fundamental 2D perovskite architecture, with corner-sharing inorganic octahedra separated by organic bilayers (Fig. 5). Significant disorder is observed within the inorganic framework, with each halide site exhibiting equal probability of bromide or chloride occupancy. Within the organic layers, disorder also arises from symmetry-related configurations. In $[BA]_2PbBr_2Cl_2$, the butylammonium cation adopts four orientations due to its rotational symmetry. Similarly, in $[MeTzEA]_2PbBr_2Cl_2$, the tetrazine moiety lies on a twofold rotation axis, resulting in two possible configurations. Representative configurations for each structure are shown in Fig. 5. Despite this disorder, the overall structural motifs and layer spacings are comparable to those of the corresponding chloride-based perovskites. Key crystallographic parameters are summarized in Tables S5 and S6, with full structural details provided in the SI (Fig. S14 and S15).

Structural distortions of the inorganic framework, such as octahedral tilting, are known to influence optical properties in 2D hybrid perovskites. In the mixed-anion series, differences in spacer-cation size and connectivity are expected to introduce some variation in lattice structure. However, due to substantial halide disorder in the inorganic layers of the mixed-anion systems, extraction of rigorous distortion metrics from the available crystal structures is not feasible.

Band alignment in chloride and mixed-anion 2D OIHPs

To gain qualitative insight into spacer-cation dependent electronic structure, we performed first-principles electronic

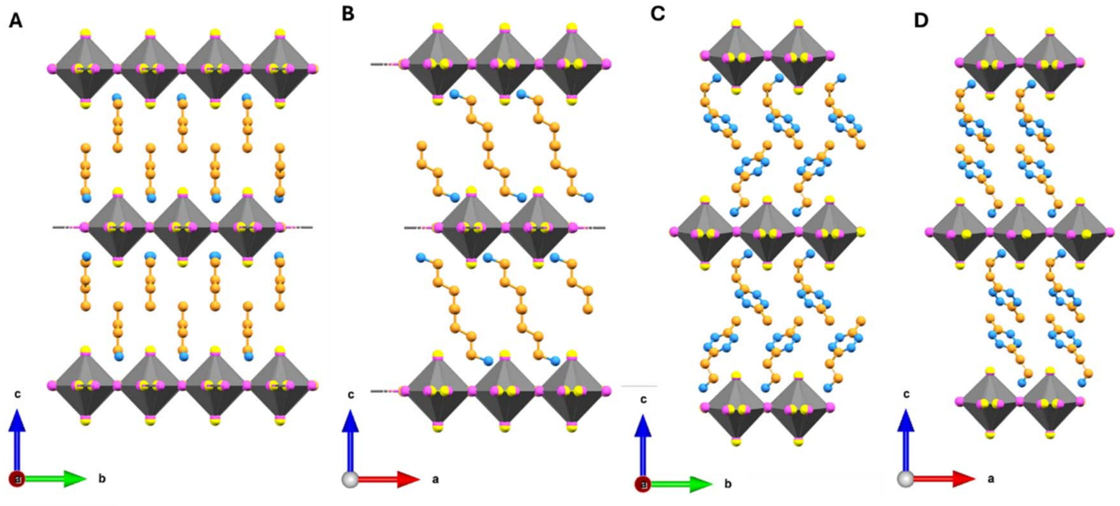

Fig. 5 Side view of the crystal structures. $[BA]_2PbBr_2Cl_2$ viewed down (A) *a*-axis and (B) *b*-axis. $[MeTzEA]_2PbBr_2Cl_2$ viewed down (C) *a*-axis and (D) *b*-axis. Hydrogen atoms are omitted for clarity. Cl, magenta; Br, yellow; C, orange; N, blue; gray diamonds within inorganic layers represent octahedral $[PbBr_3Cl_3]^{4-}$.

Open Access Article. Published on 13 May 2026. Downloaded on 6/3/2026 11:05:26 AM.
This article is licensed under a Creative Commons Attribution 3.0 Unported Licence.

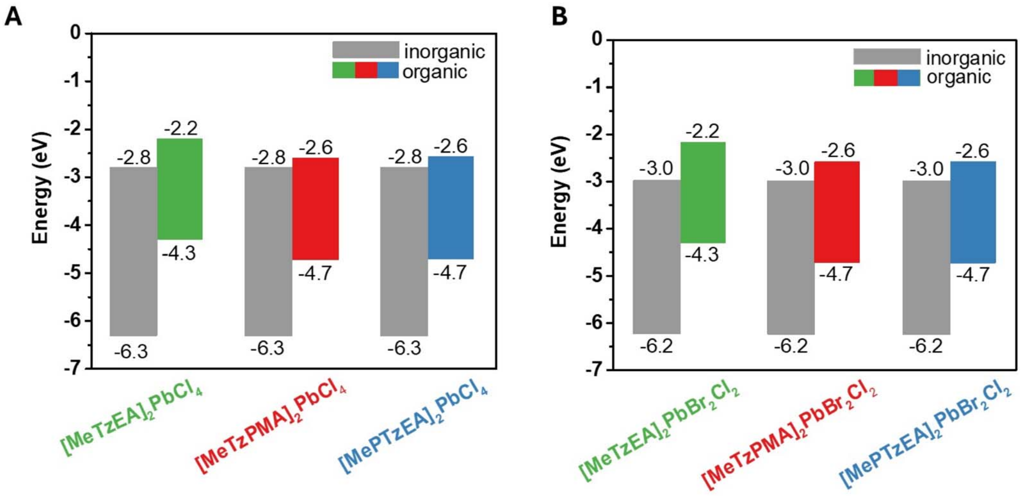

Fig. 6 Band alignment diagrams of inorganic and organic components as determined from UPS and optical absorption measurements. (A) Lead chloride-based 2D OIHPs and (B) mixed-anion 2D OIHPs, showing inorganic (gray) and organic (green, red, blue) components.

structure calculations for [MePTzEA]$_2$PbCl$_4$ using density functional theory (DFT) with the all-electron FHI-aims code, as described in our previous work.[46] These calculations indicate that the valence-band edge has significant contribution from the organic cation, while the conduction-band edge is primarily associated with the inorganic sublattice (Fig. S20C). This calculated band ordering is consistent with a staggered, type-IIa quantum-well configuration for [MePTzEA]$_2$PbCl$_4$ (Fig. S20F). While DFT calculations provide useful qualitative insight into how the electronic structure of the spacer-cation can influence frontier electronic states, it is important to note that DFT calculations are performed on the fully integrated hybrid structure and therefore reflect the electronic structure of the coupled organic–inorganic system. As a result, the calculated band alignment can differ from experimentally derived alignments based on measurements of the individual components. Furthermore, extension of the DFT analysis to other chloride and mixed-anion compositions is limited by substantial structural disorder within the organic layers. Additional computational details are provided in the SI (Fig. S20).

To experimentally probe band alignment in both chloride and mixed-anion systems, ultraviolet photoelectron spectroscopy (UPS) was employed.[8,50] Because UPS directly probes the electronic structure of thin films, these measurements are taken as the primary experimental basis for constructing the band alignment diagrams discussed below. As an inorganic reference, we utilized [BA]$_2$PbCl$_4$, a system with a known type-Ib alignment, to probe the electronic states of the inorganic framework. UPS measurements yield a valence band maximum of approximately −6.3 eV for [BA]$_2$PbCl$_4$ (Fig. S21). Similarly, [BA]$_2$PbBr$_2$Cl$_2$ was used as an inorganic reference for the mixed-anion systems, with a measured valence-band maximum of approximately −6.2 eV (Fig. S21).

Because the electronic states near the band edges in lead halide perovskites are dominated by the Pb–X framework, similar inorganic sublattices are expected to exhibit comparable band edge energies, although subtle differences arising from octahedral tilting and local disorder may lead to small variations in band energies.[8,51] Accordingly, the tetrazine-based perovskites are expected to have inorganic band-edge energies similar to those of their BA-based counterparts. While valence band positions were determined directly from UPS measurements, conduction band energies were estimated from the optical band gaps of BA-based 2D perovskites obtained from UV-Vis spectroscopy.

The HOMO energy levels of the organic cations, MeTzEA, MePTzEA, and MeTzPMA, were determined from UPS measurements on thin films containing only the corresponding organic chloride salts. The measured HOMO energies are −4.3 eV for MeTzEA and −4.7 eV for both MePTzEA and MeTzPMA (Fig. S22). The similar HOMO level of MePTzEA and MeTzPMA is expected since exchanging the relative positions of donor and acceptor moieties is not anticipated to substantially alter the frontier orbital energies. The optical gap from the UV-Vis spectra of the tetrazine salts was used to infer the LUMO energy levels. The resulting band diagrams (Fig. 6), constructed primarily from UPS and optical measurements, are consistent with a type-IIb band alignment in both the chloride and mixed-anion OIHPs, in which the valence band is associated with the organic component and the conduction band is dominated by the inorganic framework.

Spacer-cation dependent excited state quenching

To investigate how the band alignment influences excited-state relaxation pathways at the organic–inorganic interface, we applied a combination of spectroscopic techniques to mixed-anion 2D OIHP thin films. Photoexcitation of the perovskite quantum wells can result in energy- or charge-transfer quenching, depending on the electronic structure of the incorporated tetrazine spacer-cation. Steady-state photoluminescence (PL) measurements can establish quenching

Open Access Article. Published on 13 May 2026. Downloaded on 6/3/2026 11:05:26 AM.
This article is licensed under a Creative Commons Attribution 3.0 Unported Licence.

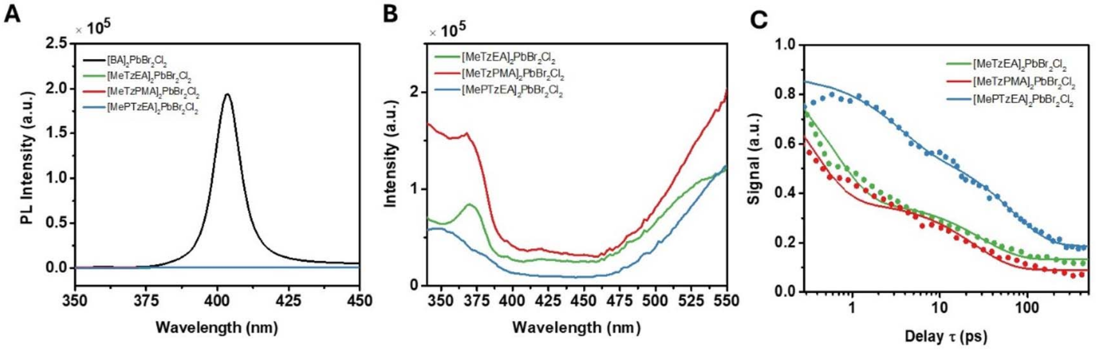

Fig. 7 (A) Photoluminescence (PL) spectra for $[BA]_2PbBr_2Cl_2$ (black), $[MeTzEA]_2PbBr_2Cl_2$ (green), $[MeTzPMA]_2PbBr_2Cl_2$ (red), and $[MePTzEA]_2PbBr_2Cl_2$ (blue) films excited at 320 nm. (B) Photoluminescence excitation spectra for $[MeTzEA]_2PbBr_2Cl_2$ (green), $[MeTzPMA]_2PbBr_2Cl_2$ (red), and $[MePTzEA]_2PbBr_2Cl_2$ (blue), monitored at a fixed emission wavelength of 600 nm corresponding to the tetrazine emission. (C) Absolute values of transient grating signal fields acquired for $[MeTzEA]_2PbBr_2Cl_2$ (green), $[MeTzPMA]_2PbBr_2Cl_2$ (red), and $[MePTzEA]_2PbBr_2Cl_2$ (blue). Dotted and solid lines represent experimental data and fits using eqn (1), respectively. Additional experimental details are provided in the SI (Fig. S24).

processes and offer initial insight into the operative excited-state pathways.

To first establish whether quenching of the inorganic exciton occurs, the inorganic framework was selectively photoexcited at 320 nm, and emission was monitored in the 350–450 nm spectral region corresponding to the inorganic exciton resonance (Fig. 7A). Quenching behavior in the tetrazine-based 2D OIHP thin films was compared to $[BA]_2PbBr_2Cl_2$; the latter serves as a reference system that lacks energy- or charge-transfer pathways due to its type-Ib band alignment. While photoluminescence from the inorganic framework is readily detected in $[BA]_2PbBr_2Cl_2$, we do not observe light emission from the inorganic phase for the three tetrazine-based systems, implying that the radiative recombination efficiency is reduced by at least two orders of magnitude. Complementary PL spectra in the 550–700 nm region under 375 nm excitation is provided in the SI (Fig. S23).

Based on the experimentally determined type-II band alignment (see Fig. 6B), quenching of the inorganic emission may proceed *via* either energy transfer or charge transfer pathways. Given the limited spectral overlap between tetrazine absorption and the ∼380 nm inorganic exciton, Förster-type dipole–dipole coupling is expected to be inefficient; thus, short-range mechanisms (*e.g.*, Dexter-type transfer) remain plausible. However, charge-transfer-mediated quenching is also energetically allowed under the type-II alignment, motivating the use of additional spectroscopic methods to identify the dominant relaxation pathway(s).

To disentangle these two possible mechanisms (*e.g.*, energy transfer *vs.* charge transfer), we recorded photoluminescence excitation (PLE) profiles while monitoring emission at 600 nm (Fig. 7B). Because the detection wavelength corresponds to light emission from the tetrazine cations, the PLE spectrum should mirror the absorption spectrum of the perovskite quantum well if an inorganic-to-organic energy transfer process precedes emission. Although both components absorb within the scanned excitation window, the perovskite quantum wells exhibit distinct, narrow exciton resonances near 380 nm. Thus, the presence (or absence) of a ∼380 nm feature in the PLE spectrum provides a diagnostic of whether excitation of the inorganic layer contributes to the observed tetrazine emission. Experimentally, prominent inorganic exciton peaks were observed in the excitation profiles of both MeTzEA- and MeTzPMA-based systems, consistent with inorganic-to-organic energy transfer following photoexcitation of the perovskite quantum wells (Fig. 7B). In contrast, the absence of a perovskite exciton resonance in the PLE profile for the MePTzEA-based system suggests that the observed tetrazine emission primarily arises from direct excitation of the organic cation, with minimal contribution from inorganic-to-organic energy transfer. Together with strong quenching of inorganic emission, these observations suggest that excited-state quenching in the MePTzEA-based system is dominated by charge-transfer

Table 1 Transient grating fitting parameters

[a]Parameters	$[MePTzEA]_2PbBr_2Cl_2$	$[MeTzPMA]_2PbBr_2Cl_2$	$[MeTzEA]_2PbBr_2Cl_2$
A_1	0.313 ± 0.011	0.591 ± 0.014	0.633 ± 0.012
t_1 (ps)	2.35 ± 0.19	0.38 ± 0.02	0.48 ± 0.02
A_2	0.433 ± 0.006	0.300 ± 0.005	0.229 ± 0.004
t_2 (ps)	58.29 ± 2.15	27.64 ± 1.02	32.17 ± 1.44
A_3	0.158 ± 0.003	0.092 ± 0.002	0.121 ± 0.002
[b]t_{quench} (ps)	25.99 ± 1.01	8.52 ± 0.33	7.68 ± 0.36

[a] The mean values and standard errors are averaged over two independent transient grating data sets. [b] Quenching times are computed using eqn (2).

This journal is © The Royal Society of Chemistry 2026

Open Access Article. Published on 13 May 2026. Downloaded on 6/3/2026 11:05:26 AM.
This article is licensed under a Creative Commons Attribution 3.0 Unported Licence.

pathways, with minimal contribution from inorganic-to-organic energy transfer.

To obtain further insight into the relaxation processes, we conducted femtosecond transient grating (TG) experiments with 375 nm pump and probe laser pulses tuned into the exciton resonances of the 2D OIHP systems (see SI, Section 8.3). As described in our previous work,[52,53] the signal fields were detected using spectral interferometry to enhance sensitivity to the excited-state populations, which are directly proportional to field amplitudes obtained in this approach. In Fig. 7C, the absolute value of the signal field was fit to the sum of three components:

$$S(\tau) = A_1 \exp(-\tau/t_1) + A_2 \exp(-\tau/t_2) + A_3 \tag{1}$$

where τ is the pump–probe delay time. All fitting parameters are summarized in Table 1. Because relaxation in these films need not be strictly single exponential, t_1 and t_2 are treated here as empirical time constants that capture the overall decay dynamics rather than being uniquely assigned to specific microscopic processes. For example, simultaneous quenching and solvation dynamics can cause the signal's temporal profile to deviate from a single-exponential form,[54,55] with both time constants sensitive to the quenching processes. Furthermore, we compute an empirical quenching time, t_{quench}, using a weighted average of the two decay components:

$$t_{\text{quench}} = \frac{A_1 t_1 + A_2 t_2}{A_1 + A_2} \tag{2}$$

The $[\text{MeTzEA}]_2\text{PbBr}_2\text{Cl}_2$ ($t_{\text{quench}} = 7.7$ ps) and $[\text{MeTzPMA}]_2\text{PbBr}_2\text{Cl}_2$ ($t_{\text{quench}} = 8.5$ ps) films exhibit similar decay times, whereas the relaxation rate of $[\text{MePTzEA}]_2\text{PbBr}_2\text{Cl}_2$ is approximately three times slower ($t_{\text{quench}} = 26$ ps). This variation in quenching times reflects differences in the underlying excited-state relaxation pathways. In general, shorter quenching times arise from (i) more favorable energy level alignment between the inorganic sublattice and the organic spacer cation and (ii) stronger donor–acceptor electronic coupling across the interface. While these factors cannot be directly predicted from molecular structure alone, the spectroscopic results indicate that $[\text{MeTzEA}]_2\text{PbBr}_2\text{Cl}_2$ and $[\text{MeTzPMA}]_2\text{PbBr}_2\text{Cl}_2$ access both energy-transfer and charge-transfer pathways, whereas $[\text{MePTzEA}]_2\text{PbBr}_2\text{Cl}_2$ is dominated by charge transfer, leading to comparatively slower relaxation.

While the PLE profiles provide clear evidence for inorganic-to-organic energy transfer in $[\text{MeTzPMA}]_2\text{PbBr}_2\text{Cl}_2$ and $[\text{MeTzEA}]_2\text{PbBr}_2\text{Cl}_2$, the tetrazine cations exhibit weak absorption in the 370–400 nm region associated with the inorganic exciton resonance, suggesting that Förster-type dipole–dipole energy transfer is inefficient under these conditions. Accordingly, short-range energy transfer mechanisms such as Dexter-type transfer are plausible in these systems, as they proceed *via* electron exchange enabled by wavefunction overlap at the organic–inorganic interface and do not require strong optical absorption by the acceptor.[56,57] Notably, excited-state quenching in a closely related tetrazine-based mixed-anion 2D OIHP system was previously attributed to Dexter energy transfer for similar reasons.[44] To provide physical context for the observed trends, we consider idealized rate expressions for Dexter energy transfer and charge transfer, which highlight the distinct energetic and coupling requirements of these processes. To clarify the factors governing the Dexter process, we derive a perturbative rate formula using a time-correlation function approach in the SI, Section 9.1. Under the assumption of Gaussian spectral line shapes, the Dexter rate can be written as

$$k_{\text{Dexter}} = \frac{|V_{\text{Dexter}}|^2}{\hbar}\sqrt{\frac{\pi}{k_B T(\lambda_D + \lambda_A)}}\exp\left[-\frac{(E_D - \lambda_D - E_A - \lambda_A)^2}{4(\lambda_D + \lambda_A)k_B T}\right] \tag{3}$$

where V_{Dexter} is the donor–acceptor coupling, E_D (E_A) is the energy gap of the donor (acceptor), and λ_D (λ_A) is the reorganization energy of the donor (acceptor). Provided sufficient interfacial wavefunction overlap to enable Dexter coupling, the efficiency of the process is governed by the energetic resonance between donor and acceptor gaps, which reflects both their mean values (E_D and E_A) and their thermally broadened distributions (λ_D and λ_A).

In contrast, the $[\text{MePTzEA}]_2\text{PbBr}_2\text{Cl}_2$ system undergoes a strong quenching process but does not exhibit signatures of energy transfer in the PLE profile. This combination is consistent with a quenching pathway dominated by charge-transfer-mediated relaxation rather than energy transfer. Given the type-II energy level scheme presented in Fig. 6, inorganic-to-organic hole transfer is energetically plausible in this system. Under the assumption that a single occupied molecular orbital serves as a dominant hole-acceptor state, the rate can be approximated using the high-temperature limit of the Marcus equation:[58,59]

$$k_{\text{Marcus}} = \frac{|V_{\text{Marcus}}|^2}{\hbar}\sqrt{\frac{\pi}{\lambda k_B T}}\exp\left[-\frac{(\Delta G + \lambda)}{4\lambda k_B T}\right], \tag{4}$$

where V_{Marcus} is the donor–acceptor coupling, ΔG is the free energy difference between donor and acceptor levels, and λ is the overall reorganization energy for the transition.

While both Dexter and Marcus couplings are mediated by wavefunction overlap at the interface, the two processes involve different energetic requirements. The energy level scheme shown in Fig. 8A illustrates the resonance condition required for Dexter energy transfer in $[\text{MeTzPMA}]_2\text{PbBr}_2\text{Cl}_2$ and $[\text{MeTzEA}]_2\text{PbBr}_2\text{Cl}_2$. Here, we propose that a higher-lying acceptor gap within the tetrazine manifold (*e.g.*, between the nonbonding orbital and a higher-energy unoccupied π orbital) can serve as the accepting transition for Dexter-type transfer, consistent with the weak absorptivity of transitions originating from nonbonding orbitals. Conversely, for $[\text{MePTzEA}]_2\text{PbBr}_2\text{Cl}_2$, the absence of an energy-transfer signature in PLE suggests that there is not an available resonant state required for Dexter energy transfer (Fig. 8B). Rather, we propose that occupied orbitals in the vicinity of the valence band edge of the perovskite layer act as the acceptor levels for the charge-transfer quenching

Open Access Article. Published on 13 May 2026. Downloaded on 6/3/2026 11:05:26 AM.
This article is licensed under a Creative Commons Attribution 3.0 Unported Licence.

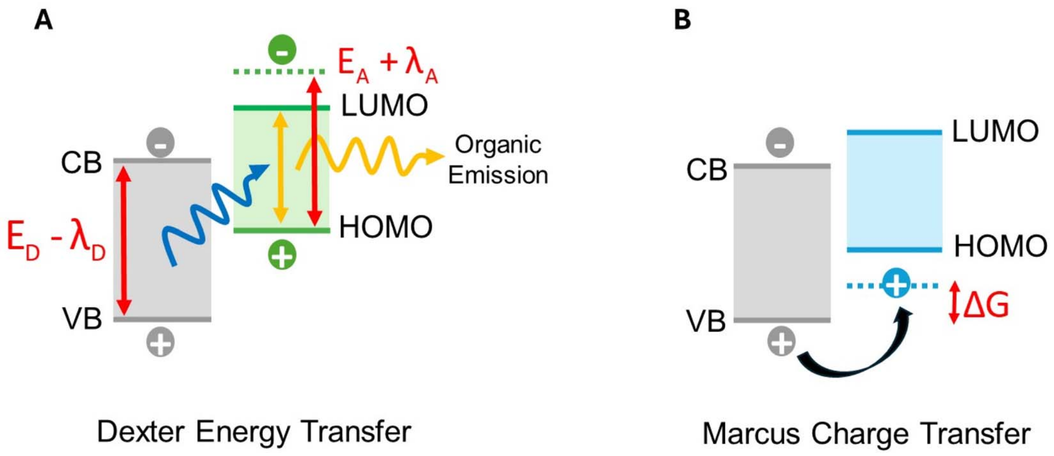

Fig. 8 (A) Dexter energy transfer occurs between the perovskite and tetrazine derivatives due to orbital overlap at the interface. Energy transfer processes are enabled by overlapping distributions of energy gaps at the donor and acceptor sites (*i.e.*, band alignment is not required). Whereas the HOMO–LUMO gap is smaller than the perovskite exciton resonance, the gap between HOMO and the levels above LUMO can accept the energy from the perovskite. (B) Charge transfer processes require energy level alignment at the interfaces of the donor and acceptor systems. Because the energy levels in the tetrazine system are discrete, we assume a single dominant hole-acceptor level to estimate the coupling strength.

process in $[\mathrm{MePTzEA}]_2\mathrm{PbBr}_2\mathrm{Cl}_2$, consistent with the energy-level scheme established by our UPS measurements. While these interpretations are supported by experimental data and idealized rate formulas, additional electronic structure calculations will enable a more detailed assignment of the specific orbitals participating in these pathways, which will be the focus of future investigation.

Design implications and summary

Overall, UPS measurements indicate a type-IIb band alignment across all tetrazine-based 2D OIHP systems investigated here. Steady-state photoluminescence (PL) studies further reveal strong quenching of the inorganic emission, consistent with the presence of charge- and/or energy-transfer processes. To distinguish between these pathways, we employed photoluminescence excitation (PLE) and transient grating (TG) spectroscopy. Together, the PLE and TG measurements provide complementary evidence that excited-state relaxation in $[\mathrm{MeTzPMA}]_2\mathrm{PbBr}_2\mathrm{Cl}_2$ and $[\mathrm{MeTzEA}]_2\mathrm{PbBr}_2\mathrm{Cl}_2$ is consistent with Dexter-type energy transfer occurring in competition with charge separation, whereas $[\mathrm{MePTzEA}]_2\mathrm{PbBr}_2\mathrm{Cl}_2$ is dominated by charge-transfer pathways. Given all three tetrazine-based spacer-cations are structurally related, these results highlight spacer-cation electronic structure and connectivity as key parameters for influencing excited-state relaxation pathways in 2D hybrid perovskites, particularly in systems where short-range interfacial coupling is present.

Conclusions

This work establishes tetrazine-based spacer-cations as a distinct and effective design motif for engineering excited-state pathways in two-dimensional organic–inorganic hybrid perovskites. By combining compact molecular size with intrinsically narrow optical gaps, tetrazine derivatives overcome a longstanding limitation in 2D OIHP design, where reduced band gaps are typically achieved only through extended conjugation that requires bulky solubilizing substituents. As a result, tetrazines provide access to interfacial electronic structures that are difficult to reach using more conventional conjugated spacer-cations.

Beyond enabling type-II band alignment, our results demonstrate that subtle differences in spacer-cation electronic structure can influence the balance between competing excited-state relaxation pathways. In particular, the availability of low-oscillator-strength tetrazine excited states appears to facilitate short-range, Dexter-type energy transfer in certain systems, whereas changes in conjugation and connectivity can suppress energy transfer and favor charge separation instead. These findings highlight that excited-state dynamics in 2D OIHPs are governed not only by energetic alignment, but also by the detailed structure of the organic excited-state manifold and its coupling to the inorganic framework, providing a key design parameter for tuning excited-state relaxation pathways in layered hybrid perovskites.

More broadly, this study underscores spacer-cation electronic structure as a powerful and tunable parameter for controlling short-range interfacial coupling in layered hybrid perovskites. By deliberately selecting or designing organic cations with tailored excited-state properties, it should be possible to rationally enhance or suppress energy transfer, promote charge separation, or access hybrid excited states with mixed organic–inorganic character. Such control will be essential for optimizing 2D OIHPs for optoelectronic applications ranging from light harvesting to charge-transport and excitonic devices.

Author contributions

CJG, AMM and WY conceived the idea. JS and JH synthesized the cations. CJG fabricated all perovskites (crystals and thin films). ZG conducted the spectroscopic studies. WAH and CHC

Open Access Article. Published on 13 May 2026. Downloaded on 6/3/2026 11:05:26 AM. This article is licensed under a Creative Commons Attribution 3.0 Unported Licence.

resolved the crystal structures. SB and YK conducted the computational study. LY conducted the UPS study and facilitated the growth of single crystals and thin films. AMM and WY supervised and coordinated the entire study. The manuscript was written through contributions of all authors. All authors have given approval to the final version of the manuscript.

Conflicts of interest

There are no conflicts to declare.

Data availability

CCDC 2472020–2472022, 2493561 and 2493562 contain the supplementary crystallographic data for this paper.[60a–e]

The data supporting this article have been included as part of the manuscript and the supplementary information (SI). Supplementary information: experimental procedures, including all syntheses and NMR spectra of organic cations, fabrication and characterization of thin films and crystals, including details concerning single crystal XRD, thin film pXRD, UV-Vis absorption spectra, UPS spectra, optical spectroscopy, and computational experiments. Additional views of solved crystal structures and key crystallographic details are available as well. Additional discussion of perturbative rate models for Dexter energy transfer and charge transfer is provided to clarify the physical interpretation of the spectroscopic trends. See DOI: https://doi.org/10.1039/d6ta01590e.

Acknowledgements

This work is supported by the National Science Foundation (NSF) Graduate Research Fellowship Program (GRFP) under DGE-2439854 (for C. G.), NSF CHE-2154791 (for Z. G., J. S., W. H., A. M., and W. Y.), NSF DMR-2425696 (for S. B., L. Y., and Y. K.). W. Y and J. H. were also supported by the Center for Hybrid Organic Inorganic Semiconductors for Energy (CHOISE), an Energy Frontier Research Center funded by the U.S. Department of Energy (DOE), Office of Science, Office of Basic Energy Sciences (BES). The XRD, UPS, XPS and SEM of thin films were performed in part at the Chapel Hill Analytical and Nanofabrication Laboratory, CHANL, a member of the North Carolina Research Triangle Nanotechnology Network, RTNN, which is supported by the National Science Foundation, Grant ECCS-2025064, as part of the National Nanotechnology Coordinated Infrastructure, NNCI. A portion of this work was performed using XPS/UPS/IPES and fluorescence (Edinburgh FLS920) instrumentation supported by the Center for Hybrid Approaches in Solar Energy to Liquid Fuels (CHASE), an Energy Innovation Hub funded by the U.S. Department of Energy, Office of Science, Office of Basic Energy Sciences under Award Number DE-SC0021173. We acknowledge C. Donley for assistance with XPS and UPS measurement. We acknowledge A. Kumbhar for assistance with SEM imaging. Single crystal XRD data was collected using the University of North Carolina Department of Chemistry X-ray Crystallography Core Laboratory's Bruker D8 VENTURE diffractometer, supported by the National Science Foundation under Grant No. CHE-2117287. We also gratefully acknowledge Dr Matthias Zeller (Purdue University) for his assistance in resolving the [MeTzPMA]$_2$-PbCl$_4$·CH$_2$Cl$_2$ crystal structure.

Notes and references

1 C. R. Kagan, D. B. Mitzi and C. D. Dimitrakopoulos, *Science*, 1999, **286**, 945–947.
2 B. Saparov and D. B. Mitzi, *Chem. Rev.*, 2016, **116**, 4558–4596.
3 Z. Guo, N. Zhou, O. F. Williams, J. Hu, W. You and A. M. Moran, *J. Phys. Chem. C*, 2018, **122**, 10650–10656.
4 D. B. Straus and C. R. Kagan, *J. Phys. Chem. Lett.*, 2018, **9**, 1434–1447.
5 J. Hu, I. W. H. Oswald, H. Hu, S. J. Stuard, M. M. Nahid, L. Yan, Z. Chen, H. Ade, J. R. Neilson and W. You, *ACS Mater. Lett.*, 2019, **1**, 171–176.
6 N. Zhou, J. Hu, Z. Ouyang, O. F. Williams, L. Yan, W. You and A. M. Moran, *J. Phys. Chem. Lett.*, 2019, **10**, 7362–7367.
7 L. Yan, C. J. Gloor, A. M. Moran and W. You, *Appl. Phys. Lett.*, 2023, **122**, 240501.
8 Y. Gao, E. Shi, S. Deng, S. B. Shiring, J. M. Snaider, C. Liang, B. Yuan, R. Song, S. M. Janke, A. Liebman-Peláez, P. Yoo, M. Zeller, B. W. Boudouris, P. Liao, C. Zhu, V. Blum, Y. Yu, B. M. Savoie, L. Huang and L. Dou, *Nat. Chem.*, 2019, **11**, 1151–1157.
9 C. Liu, W. Huhn, K.-Z. Du, A. Vazquez-Mayagoitia, D. Dirkes, W. You, Y. Kanai, D. B. Mitzi and V. Blum, *Phys. Rev. Lett.*, 2018, **121**, 146401.
10 W. A. Dunlap-Shohl, E. T. Barraza, A. Barrette, S. Dovletgeldi, G. Findik, D. J. Dirkes, C. Liu, M. K. Jana, V. Blum, W. You, K. Gundogdu, A. D. Stiff-Roberts and D. B. Mitzi, *Mater. Horiz.*, 2019, **6**, 1707–1716.
11 D. B. Mitzi, K. Chondroudis and C. R. Kagan, *Inorg. Chem.*, 1999, **38**, 6246–6256.
12 H. Tsai, W. Nie, J. C. Blancon, C. C. Stoumpos, R. Asadpour, B. Harutyunyan, A. J. Neukirch, R. Verduzco, J. J. Crochet, S. Tretiak, L. Pedesseau, J. Even, M. A. Alam, G. Gupta, J. Lou, P. M. Ajayan, M. J. Bedzyk and M. G. Kanatzidis, *Nature*, 2016, **536**, 312–316.
13 L. Yan, J. Hu, Z. Guo, H. Chen, M. F. Toney, A. M. Moran and W. You, *ACS Appl. Mater. Interfaces*, 2018, **10**, 33187–33197.
14 L. Yan, M. K. Jana, P. C. Sercel, D. B. Mitzi and W. You, *J. Am. Chem. Soc.*, 2021, **143**, 18114–18120.
15 R. Zhu, J. Lai, W. Lv, J. Tan and S. Ye, *Small*, 2026, **22**, e07331.
16 C. Katan, N. Mercier and J. Even, *Chem. Rev.*, 2019, **119**, 3140–3192.
17 J. Leveillee, C. Katan, L. Zhou, A. D. Mohite, J. Even, S. Tretiak, A. Schleife and A. J. Neukirch, *Phys. Rev. Mater.*, 2018, **2**, 105406.
18 J. C. Blancon, A. V. Stier, H. Tsai, W. Nie, C. C. Stoumpos, B. Traoré, L. Pedesseau, M. Kepenekian, F. Katsutani, G. T. Noe, J. Kono, S. Tretiak, S. A. Crooker, C. Katan, M. G. Kanatzidis, J. J. Crochet, J. Even and A. D. Mohite, *Nat. Commun.*, 2018, **9**, 2254.
19 K. Ema, M. Inomata, Y. Kato, H. Kunugita and M. Era, *Phys. Rev. Lett.*, 2008, **100**, 257401.

Open Access Article. Published on 13 May 2026. Downloaded on 6/3/2026 11:05:26 AM.
This article is licensed under a Creative Commons Attribution 3.0 Unported Licence.

20 M. K. Jana, C. Liu, S. Lidin, D. J. Dirkes, W. You, V. Blum and D. B. Mitzi, *Chem. Mater.*, 2019, **31**, 8523–8532.
21 D. Han, S. Chen and M.-H. Du, *J. Phys. Chem. Lett.*, 2021, **12**, 9754–9760.
22 W. Dou, Z. Yin, Y. Zhang, H. Deng and N. Dai, *Nanomaterials*, 2022, **12**, 2556.
23 L. Zhang, X. Zhang and G. Lu, *J. Phys. Chem. Lett.*, 2020, **11**, 6982–6989.
24 S. Deng, J. M. Snaider, Y. Gao, E. Shi, L. Jin, R. D. Schaller, L. Dou and L. Huang, *J. Chem. Phys.*, 2020, **152**, 044711.
25 J. Sun, K. Wang, K. Ma, J. Y. Park, Z.-Y. Lin, B. M. Savoie and L. Dou, *J. Am. Chem. Soc.*, 2023, **145**, 20694–20715.
26 C. Lin, Y. Tang, W. Xu, P. Kumar and L. Dou, *ACS Energy Lett.*, 2024, **9**, 3877–3886.
27 W. T. M. Van Gompel, L. Lutsen and D. Vanderzande, *J. Mater. Chem. C*, 2023, **11**, 12877–12893.
28 E. Mahal, D. Roy, S. S. Manna and B. Pathak, *J. Mater. Chem. A*, 2023, **11**, 23547–23555.
29 X. Li, J. M. Hoffman and M. G. Kanatzidis, *Chem. Rev.*, 2021, **121**, 2230–2291.
30 Z. Ou, C. Wang, Z.-G. Tao, Y. Li, Z. Li, Y. Zeng, Y. Li, E. Shi, W. Chu, T. Wang and H. Xu, *Nano Lett.*, 2024, **24**, 5975–5983.
31 L. Dou, Y. Liu, Z. Hong, G. Li and Y. Yang, *Chem. Rev.*, 2015, **115**, 12633–12665.
32 W. Li, K. H. Hendriks, W. S. C. Roelofs, Y. Kim, M. M. Wienk and R. A. J. Janssen, *Adv. Mater.*, 2013, **25**, 3182–3186.
33 G. Li, W.-H. Chang and Y. Yang, *Nat. Rev. Mater.*, 2017, **2**, 17043.
34 H. Zhou, L. Yang and W. You, *Macromolecules*, 2012, **45**, 607–632.
35 T. Izumi, S. Kobashi, K. Takimiya, Y. Aso and T. Otsubo, *J. Am. Chem. Soc.*, 2003, **125**, 5286–5287.
36 R. L. Elsenbaumer, K. Y. Jen and R. Oboodi, *Synth. Met.*, 1986, **15**, 169–174.
37 P. Leclère, M. Surin, P. Viville, R. Lazzaroni, A. F. M. Kilbinger, O. Henze, W. J. Feast, M. Cavallini, F. Biscarini, A. P. H. J. Schenning and E. W. Meijer, *Chem. Mater.*, 2004, **16**, 4452–4466.
38 H. A. M. van Mullekom, J. A. J. M. Vekemans, E. E. Havinga and E. W. Meijer, *Mater. Sci. Eng., R*, 2001, **32**, 1–40.
39 G. Clavier and P. Audebert, *Chem. Rev.*, 2010, **110**, 3299–3314.
40 Y.-H. Gong, P. Audebert, G. Clavier, F. Miomandre, J. Tang, S. Badré, R. Méallet-Renault and E. Naidus, *New J. Chem.*, 2008, **32**, 1235–1242.
41 N. Saracoglu, *Tetrahedron*, 2007, **63**, 4199–4236.
42 A. K. Ismael and A. Al-Jobory, *R. Soc. Open Sci.*, 2024, **11**, 231533.
43 S. P. Rittmeyer and A. Groß, *Beilstein J. Nanotechnol.*, 2012, **3**, 909–919.
44 F. Lédée, P. Audebert, G. Trippé-Allard, L. Galmiche, D. Garrot, J. Marrot, J.-S. Lauret, E. Deleporte, C. Katan, J. Even and C. Quarti, *Mater. Horiz.*, 2021, **8**, 1547–1560.
45 W. Mao, W. Shi, J. Li, D. Su, X. Wang, L. Zhang, L. Pan, X. Wu and H. Wu, *Angew. Chem., Int. Ed.*, 2019, **58**, 1106–1109.
46 V. Blum, R. Gehrke, F. Hanke, P. Havu, V. Havu, X. Ren, K. Reuter and M. Scheffler, *Comput. Phys. Commun.*, 2009, **180**, 2175–2196.
47 S. Bhattacharya and Y. Kanai, *Phys. Rev. Mater.*, 2023, **7**, 055001.
48 J. Yan, H. Li, M. H. Aldamasy, C. Frasca, A. Abate, K. Zhao and Y. Hu, *Chem. Mater.*, 2023, **35**, 2683–2712.
49 M. G. McNamee, Z. Ouyang, L. Yan, Z. Gan, N. Zhou, O. F. Williams, W. You and A. M. Moran, *J. Phys. Chem. C*, 2023, **127**, 2782–2791.
50 K. Ma, J. Sun, H. R. Atapattu, B. W. Larson, H. Yang, D. Sun, K. Chen, K. Wang, Y. Lee, Y. Tang, A. Bhoopalam, L. Huang, K. R. Graham, J. Mei and L. Dou, *Sci. Adv.*, 2023, **9**, eadg0032.
51 C. Ji, S. Wang, L. Li, Z. Sun, M. Hong and J. Luo, *Adv. Funct. Mater.*, 2019, **29**, 1805038.
52 S. Feng, C. J. Badalis, C. J. Gloor, X. Zhong, Z. Gan, W. You and A. M. Moran, *J. Chem. Phys.*, 2025, **162**, 134202.
53 Z. Gan, C. J. Gloor, L. Yan, X. Zhong, W. You and A. M. Moran, *J. Chem. Phys.*, 2024, **161**, 074202.
54 B. P. Molesky and A. M. Moran, *J. Phys. Chem. A*, 2013, **117**, 13954–13966.
55 L. Li, P. G. Giokas, Y. Kanai and A. M. Moran, *J. Chem. Phys.*, 2014, **140**, 234109.
56 D. L. Dexter, *J. Chem. Phys.*, 1953, **21**, 836–850.
57 S. Yabu, H. Sato and M. Higashi, *Chem. Phys. Rev.*, 2025, **6**, 011308.
58 P. F. Barbara, T. J. Meyer and M. A. Ratner, *J. Phys. Chem.*, 1996, **100**, 13148–13168.
59 E. J. Piechota and G. J. Meyer, *J. Chem. Educ.*, 2019, **96**, 2450–2466.
60 (*a*) CCDC 2472020: Experimental Crystal Structure Determination, 2026, DOI: 10.5517/ccdc.csd.cc2nzbll.; (*b*) CCDC 2472021: Experimental Crystal Structure Determination, 2026, DOI: 10.5517/ccdc.csd.cc2nzbmm; (*c*) CCDC 2472022: Experimental Crystal Structure Determination, 2026, DOI: 10.5517/ccdc.csd.cc2nzbnn; (*d*) CCDC 2493561: Experimental Crystal Structure Determination, 2026, DOI: 10.5517/ccdc.csd.cc2pprgm; (*e*) CCDC 2493562: Experimental Crystal Structure Determination, 2026, DOI: 10.5517/ccdc.csd.cc2pprhn.